Electronic Supplementary Materials (ESI)

Energy Harvesting by Vitrimer-Based Moist-Electric Generator

Zihao Feng,[a] Wei Zhao,[*,a] Zhengxin Yang,[a] Yi Deng,[a] Tong Yang,[a] Yonghao Ni[b]

[a] College of Bioresources Chemical and Materials Engineering, Shaanxi University of Science and Technology, Xi'an 710021, P. R. China

[b] Department of Chemical Engineering, University of New Brunswick, Fredericton E3B 5A3, New Brunswick, Canada

*Correspondence to: zhwgah1028@126.com

The PDF file includes:

Supplementary Information

60% RH).

Fig. S20 Voltage output of PHU@Paper-VMEG (Cu/Cu) with different thicknesses and areas (90ºC, dripping water).

Fig. S21 Voltage output of PHU@Paper-VMEG (Al/Cu) with different thicknesses and areas (90ºC, dripping water).

Fig. S22 Scratch self-healing monitoring of PHU@Paper by polarizing microscopy (160ºC, 10s).

Fig. S23 Mechanical properties and voltage output of PHU@Paper after self-healing from damages.

Fig. S24 Effect of the line width of copper electrodes on the voltage output of PHU@Paper-VMEG with spiral electrodes.

Fig. S25 Voltage output of PHU@Paper-VMEG (Cu/Cu) with different line widths of ring-shaped electrodes.

Fig. S26 Effect of the ring number of ring-shaped copper electrodes on the voltage output of PHU@Paper-VMEG.

Fig. S27 Voltage output of PHU@Paper-VMEG (Cu/Cu) with different ring number electrodes.

Fig. S28 Voltage output of PHU@Paper-VMEG (Cu/Cu) with different patterns of electrodes. (leaf, flower, snowflake and spider web).

Fig. S29 Effect of Al electrodes on the voltage output of PHU@Paper-VMEG (Al/Cu).

Fig. S30 Voltage output of PHU@Paper-VMEG (Al/Cu) with different patterns of electrodes.

Fig. S31 Scratch self-healing monitoring of PHU@Ti_3C_2 by polarizing microscopy (160ºC, 10s).

Fig. S32 Mechanical properties and voltage output of PHU@Ti_3C_2@Paper after self-healing from damages.

Other Supplementary Materials for this manuscript include the followings:

Movie S1 PHU@Ti_3C_2 infrared thermal imaging video.

Movie S2 Electronic timer powered by four PHU@Ti_3C_2-VMEG units.

Movie S3 Electronic timer powered by two PHU@Ti_3C_2@Paper-VMEG units.

Supplementary Figures

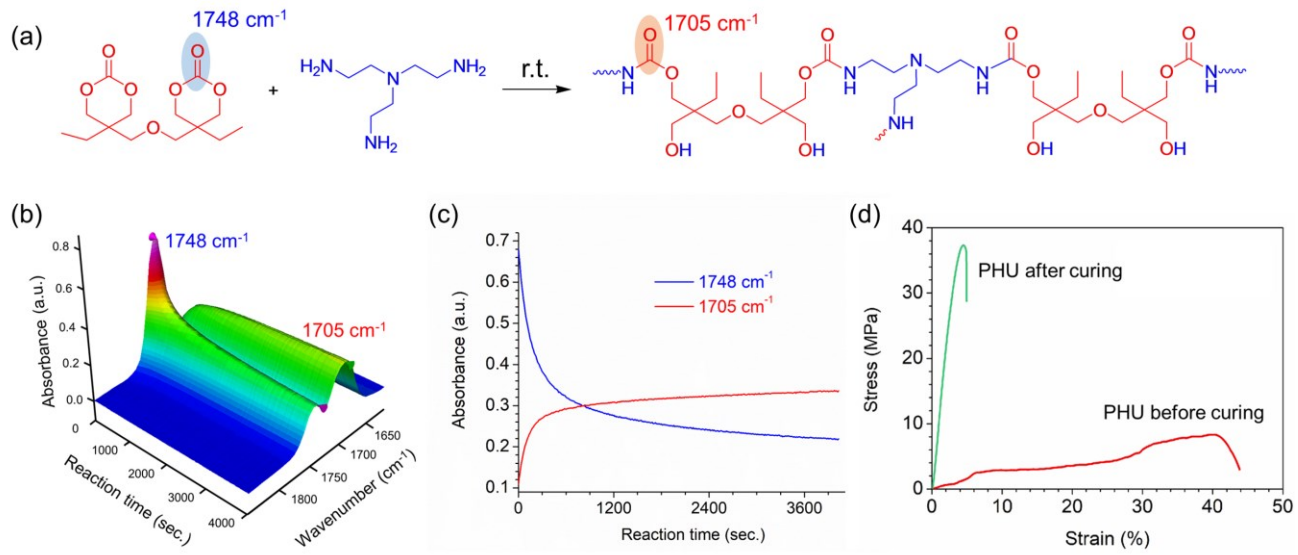

Fig. S1 *In situ* FT-IR monitoring of the reaction between BCC and TREN (conditions: [BCC]= 2.20M, [TREN]=0.73M, 25 °C, CH_2Cl_2.). (a) Reaction scheme of BCC and TREN; (b) Corresponding 3D kinetic behavior profile from *in situ* FT-IR; (c) Absorbance of 1748cm^{-1} and 1705cm^{-1} with reaction time. (d) Mechanical properties of PHU vitrimer before and after curing at 90ºC for 12 h.

Discussion of Fig. S1:

The reaction between bis(6-membered cyclic carbonate) (BCC) and tris(2-aminoethyl)amine (TREN) at room temperature was monitored by using *in situ* attenuated total reflectance (ATR) Fourier transform infrared (FT-IR) technique. An ATR diamond probe was connected to the reaction flask via AgX Fiber. Sampling was performed from 2800 to 650 cm^{-1} at 8 wavenumber resolution, and the automatic sampling interval was 10 s. The real-time concentration of BCC was quantified by measuring the intensity of the carbonyl peak of BCC at 1748 cm^{-1}. The experimental results showed that BCC could react with TREN to form PHU vitrimer at room temperature in 1 h. In addition, the mechanical property of PHU before and after heating at 90ºC for 12 h was also investigated. The

PHU after further heating at 90°C for 12 h possessed a very high strength of 37 MPa (almost 5 times higher than that of the uncured PHU), indicating further curing at a high temperature can result in dense cross-linked networks of PHU.

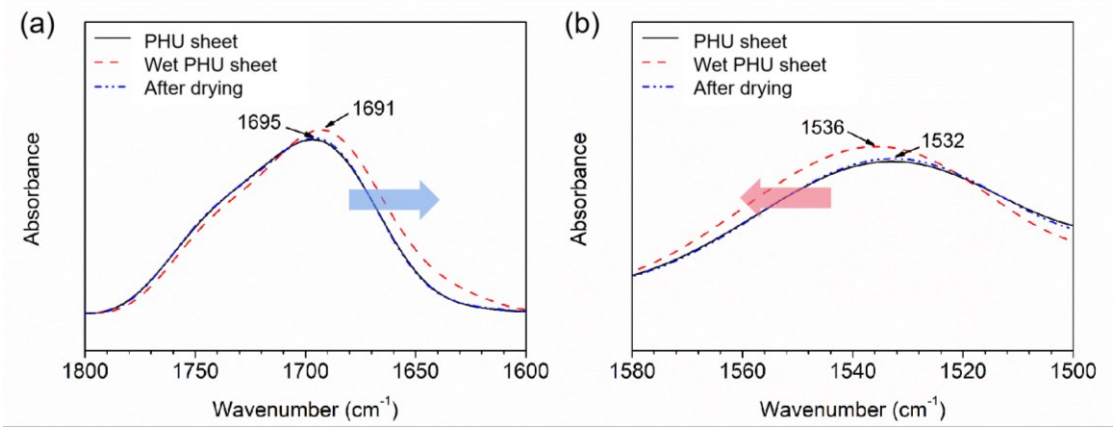

Fig. S2 ATR FI-IR spectra of the PHU film before and after water immersion. (a) Expanded N-H stretching region. (b) Expanded C=O stretching region.

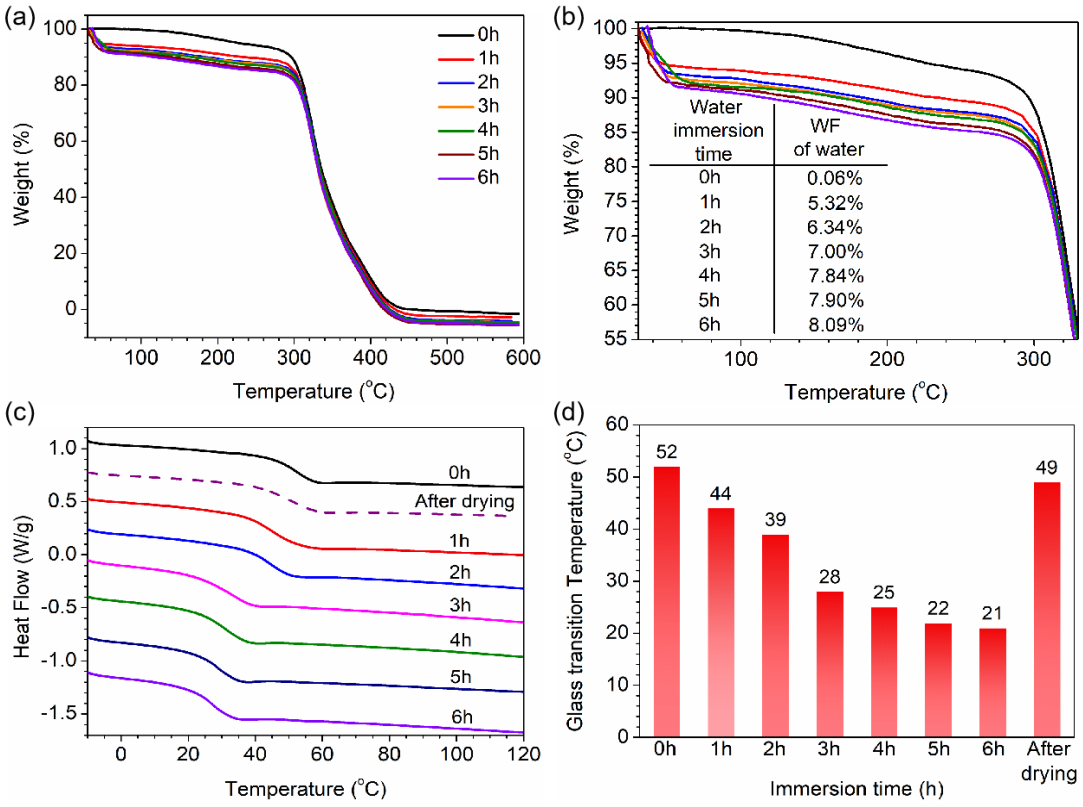

Fig. S3 TGA and DSC results of PHU after water immersion for different times. (a) TGA curves; (b) Expansion of TGA curves from 30 to 340°C; (c) DSC curves; (d) Column chart of T_g vs water immersion time.

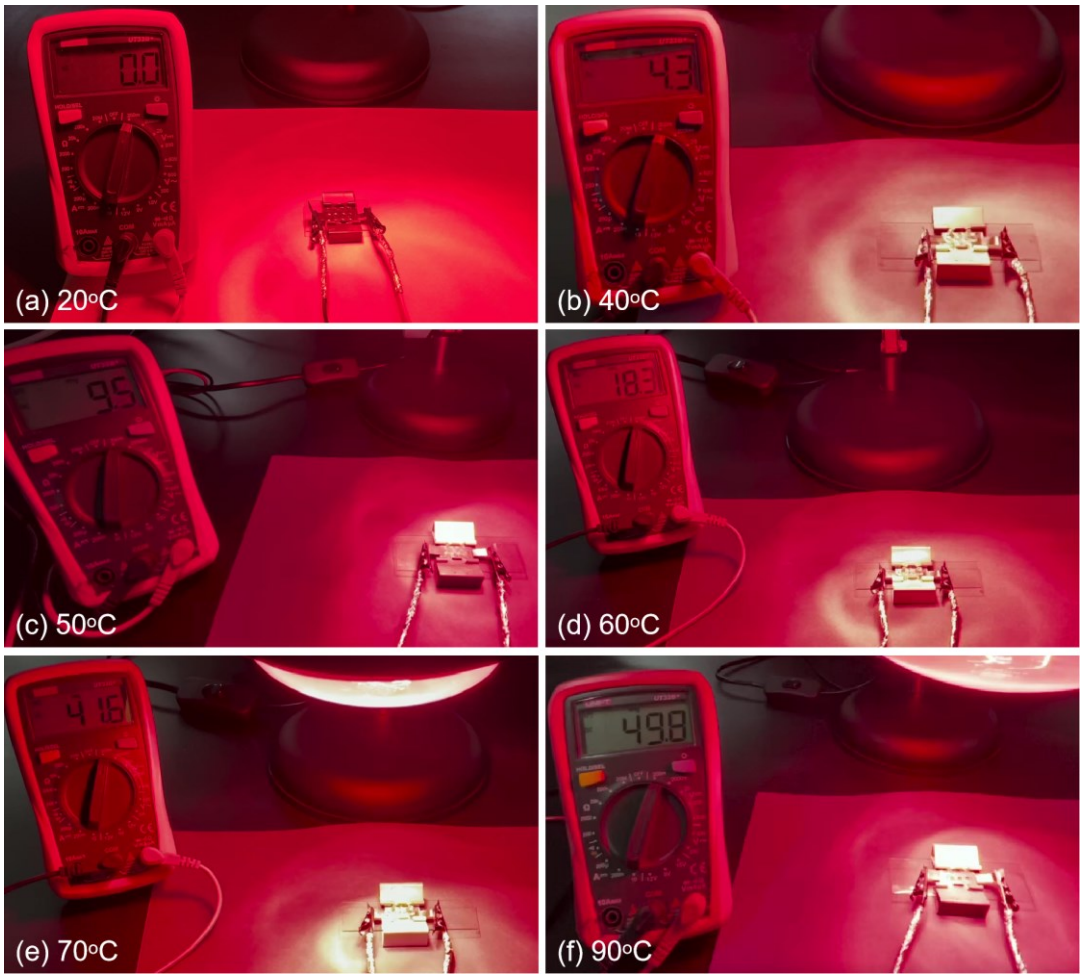

Fig. S4 Voltage output of the PHU-VMEG (Cu/Cu) at different temperatures with 60% RH (the working temperature of VMEG was adjusted by changing distance between infrared lamp and VMEG. An infrared thermometer was used to measure the working temperature of MEG).

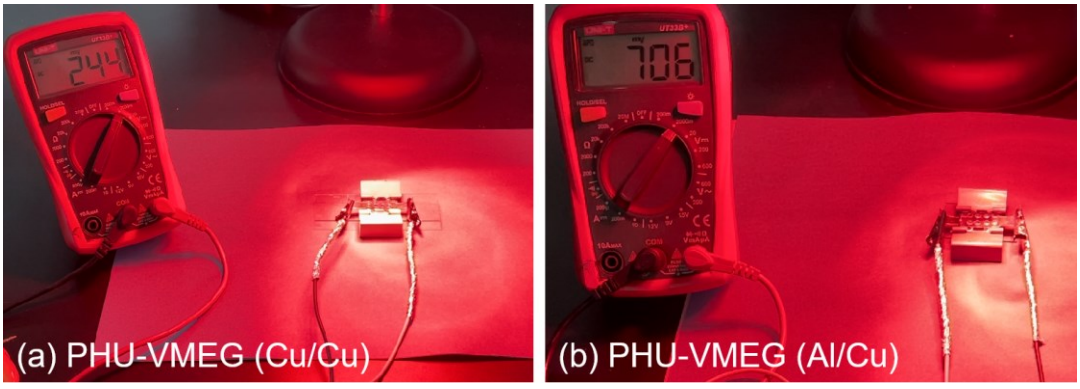

Fig. S5 Voltage output of PHU-VMEG (Cu or Al/Cu) (90°C, water dripping). (a) PHU-VMEG (Cu/Cu), (b) PHU-VMEG (Al/Cu).

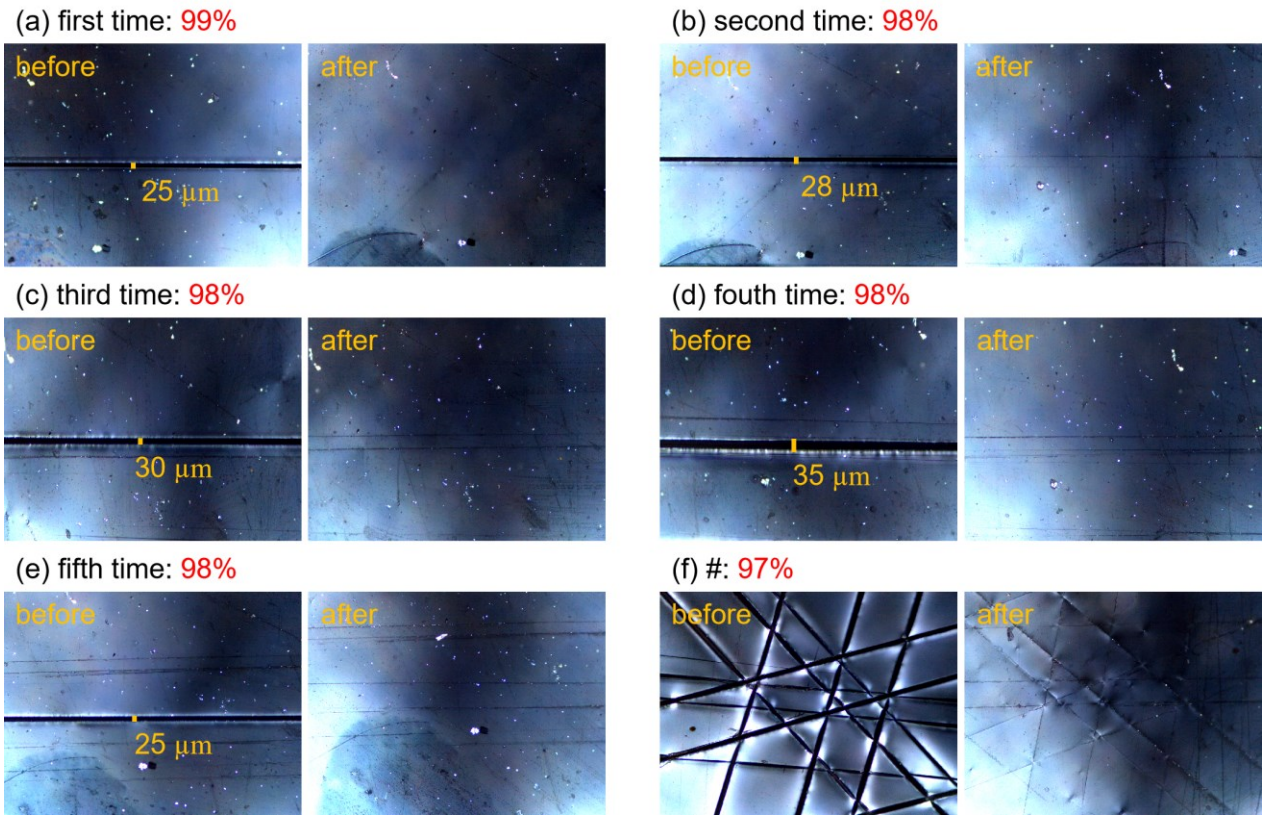

Fig. S6 Scratch self-healing monitoring of PHU at 160°C by polarizing microscopy. (a-e) five cycles of "scratch/self-healing" at roughly the same place of PHU; (f) self-healing of PHU with multiple scratches.

Discussion of Fig. S6 and Fig. S7:

Five cycles of "scratching/self-healing" were first performed at roughly the same place of PHU and the mechanical and output voltage performances of PHU after each cycle of self-healing were investigated. In addition, multiple scratches were made on the surface of PHU and the corresponding performances after self-healing were also investigated. The experimental results showed that there was only a slight decrease of the mechanical properties after self-healing and no effect on the output voltage properties was observed. This is because that covalent-bond based cross-linking networks can quickly rebuild between the damaged surfaces of PHU at a high temperature via highly efficient transcarbamoylation reactions between the hydroxyl groups (-OH) and carbamates (-NHCOO-).

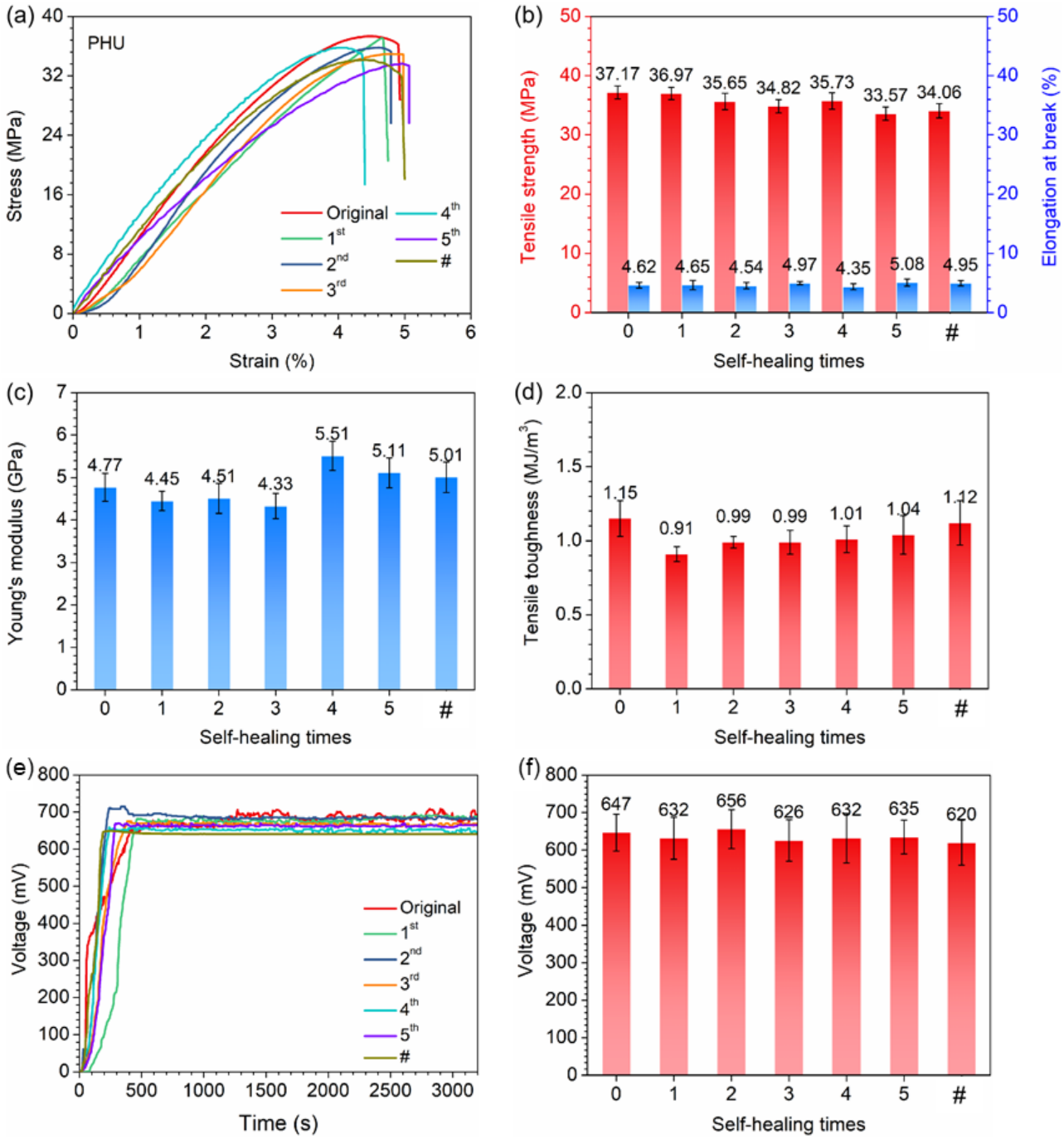

Fig. S7 (a)-(d) Mechanical properties of PHU after each cycle of self-healing in "scratching/self-healing" cycling experiments; (e) Real-time monitoring of the voltage outputs of PHU-VMEG (Al/Cu) after each cycle of self-healing; (f) Stable voltages outputs of PHU-VMEG (Al/Cu) after each cycle of self-healing.

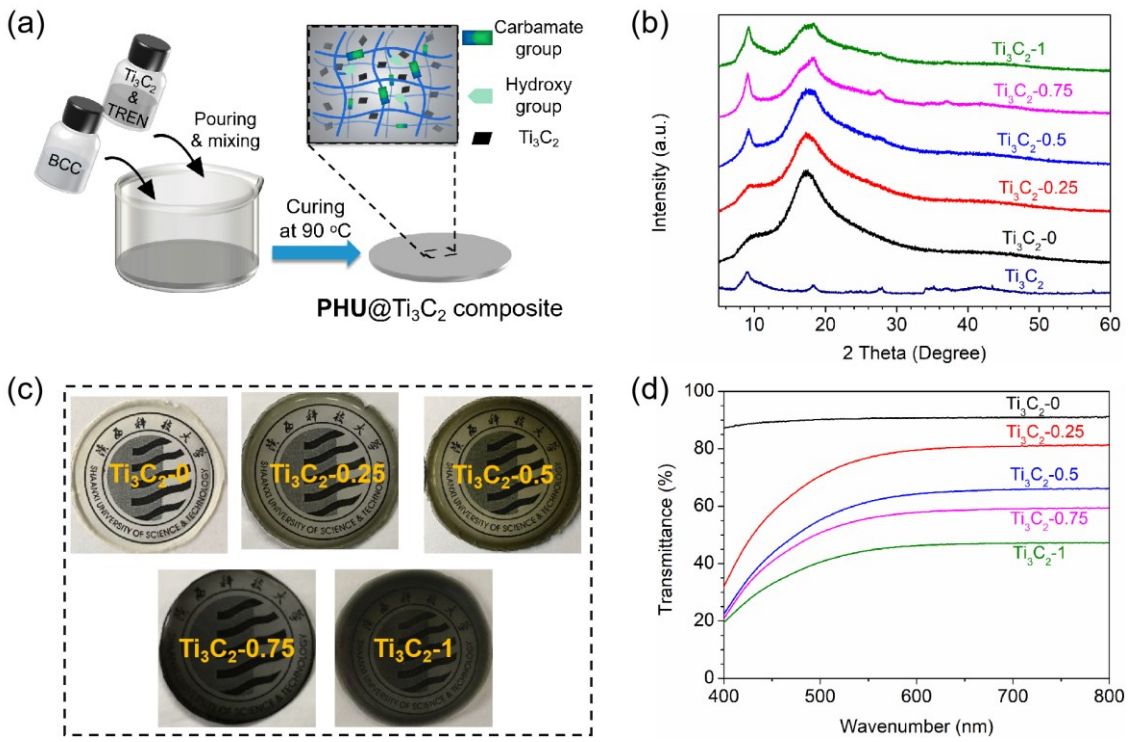

Fig. S8 Preparation and characterizations of PHU@Ti_3C_2 composite. (a) Preparation process of PHU@Ti_3C_2 composites. (b) XRD patterns for PHU, Ti_3C_2 and PHU@Ti_3C_2 composites. (c) Photographs of PHU@Ti_3C_2 composites. (d) Optical transmittance spectra of PHU@Ti_3C_2 composites.

Discussion of Fig. S8:

The PHU vitrimer composites with different contents of Ti_3C_2 (0 wt%, 0.25 wt%, 0.5 wt%, 0.75 wt% and 1 wt%) are named Ti_3C_2-0, Ti_3C_2-0.25, Ti_3C_2-0.5, Ti_3C_2-0.75 and Ti_3C_2-1 (Fig. S5). The PHU and Ti_3C_2 composites (PHU@Ti_3C_2 composites) were studied by XRD. As shown in Fig. S5b, the (002) peak intensity at 9.5° of the Ti_3C_2 in PHU@Ti_3C_2 composites augments with the increased Ti_3C_2 loading. The optical properties of the films were measured. Fig. S5d show the optical transmittance of the films with different contents of Ti_3C_2. Although the light transmittance gradually decreases with the increase in the Ti_3C_2 content, it still maintains good light transmittance in the visible light range (the average thickness of the film is 0.6mm).

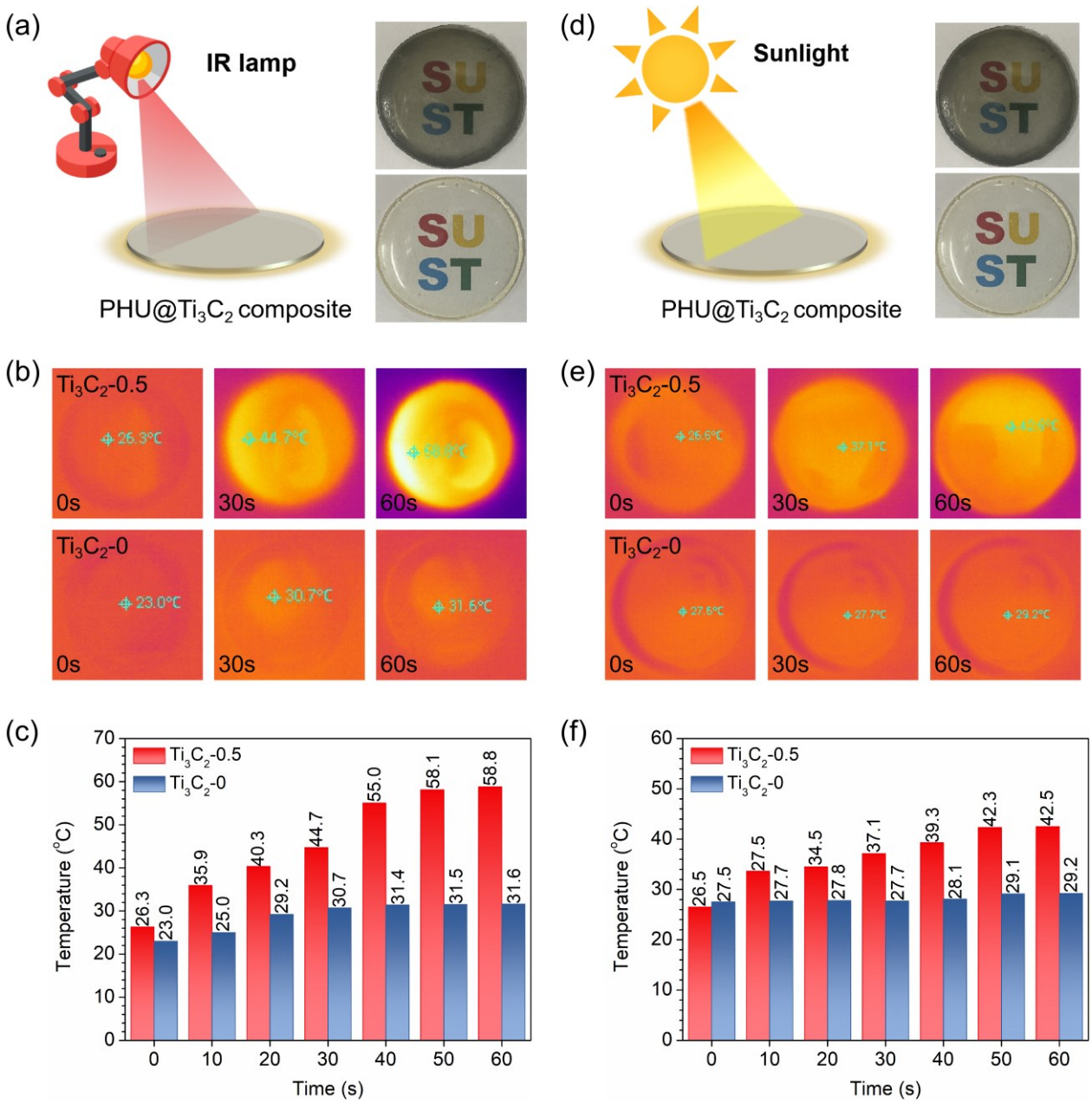

Fig. S9 Photothermal conversion effect of PHU@Ti_3C_2 composite. (a) Schematic diagram of PHU@Ti_3C_2 or PHU irradiated by IR lamp (780 nm, 100W); (b) IR images of the PHU@Ti_3C_2 and PHU taken at different times under IR radiation; (c) Temperature changes of PHU@Ti_3C_2 and PHU vs. IR radiation time.; (d) Schematic diagram of PHU@Ti_3C_2 or PHU exposed to sunlight; (e) IR images of the PHU@Ti_3C_2 and PHU taken at different times under sunlight at 1 PM (October 17, 2020, Xi'an, China, the temperature was 8 to 20ºC); (f) Temperature changes of PHU@Ti_3C_2 and PHU vs. sunlight exposure time.

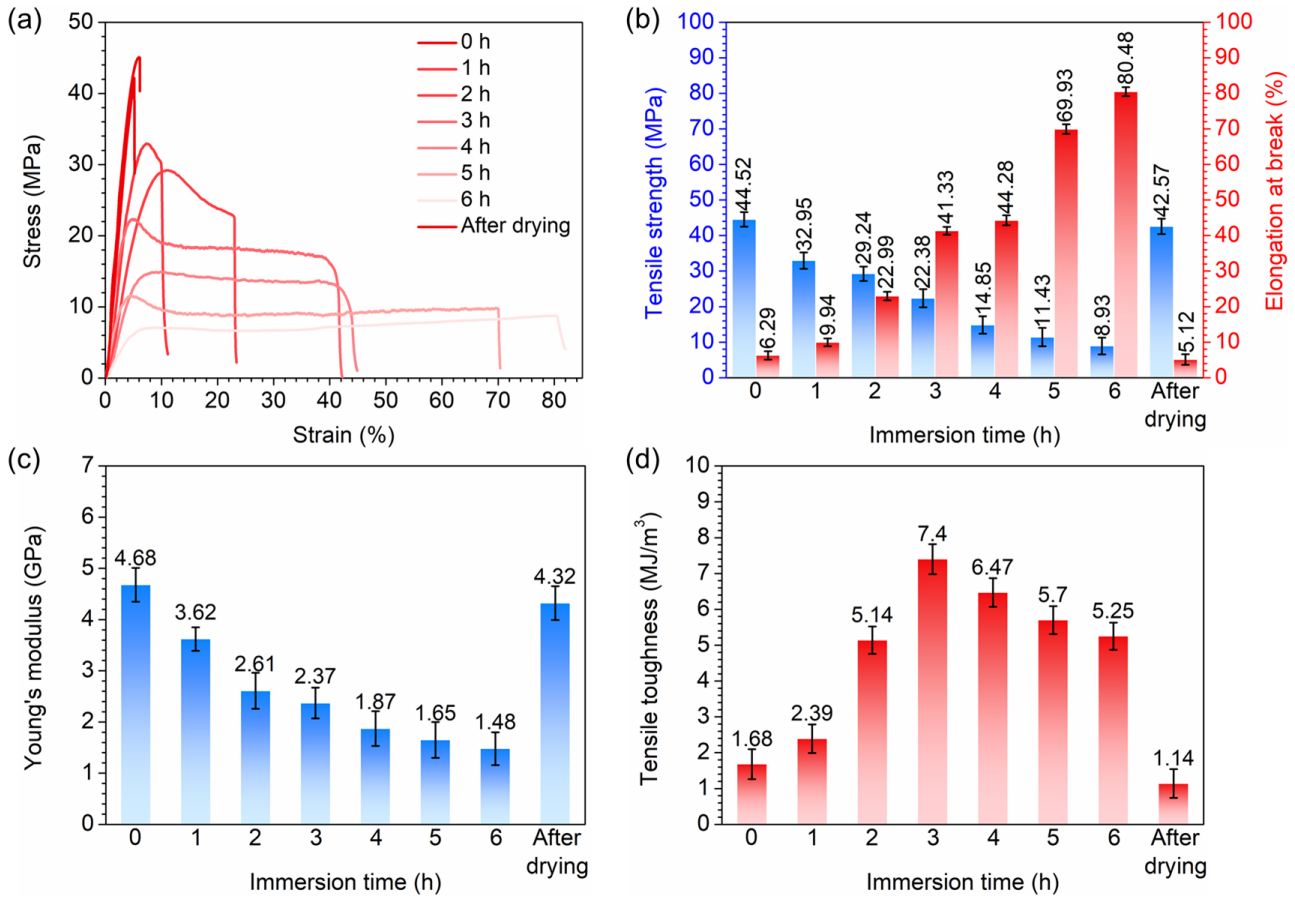

Fig. S10 Mechanical properties of PHU@Ti_3C_2 after immersion in water for different times. (a) Stress-strain relation after different hours of immersion; (b) Column chart of tensile strength and strain vs. immersion time; (c) Column chart of Young's Modulus vs. immersion time; (d) Column chart of tensile toughness vs. immersion time.

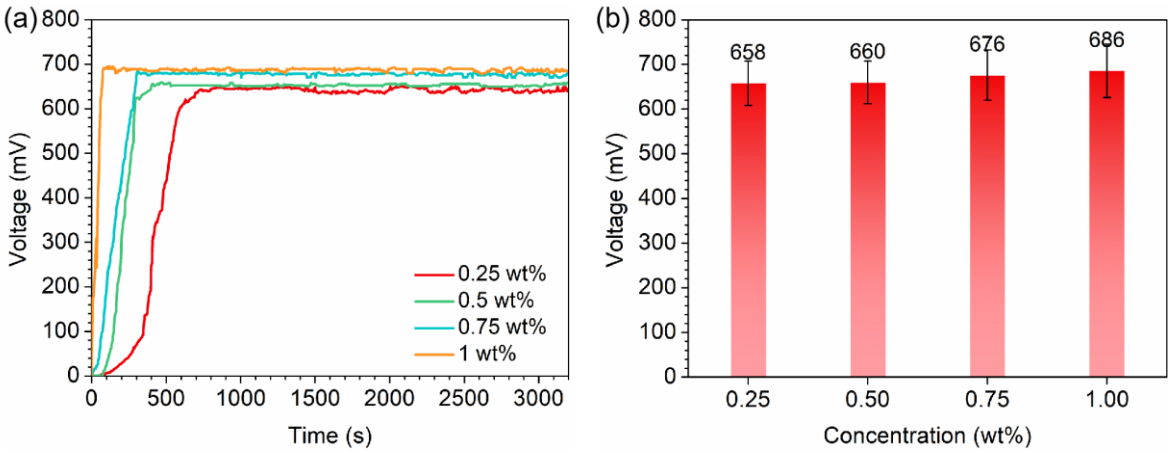

Fig. S11 Voltage outputs of PHU@Ti_3C_2 with different contents of Ti_3C_2.

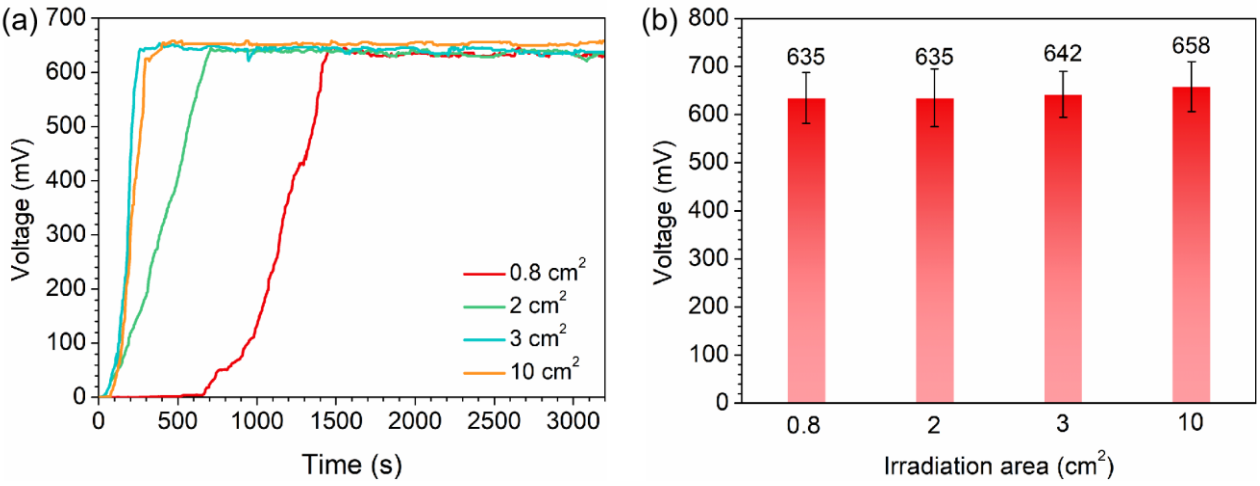

Fig. S12 Voltage outputs of PHU@Ti_3C_2 with different irradiation areas.

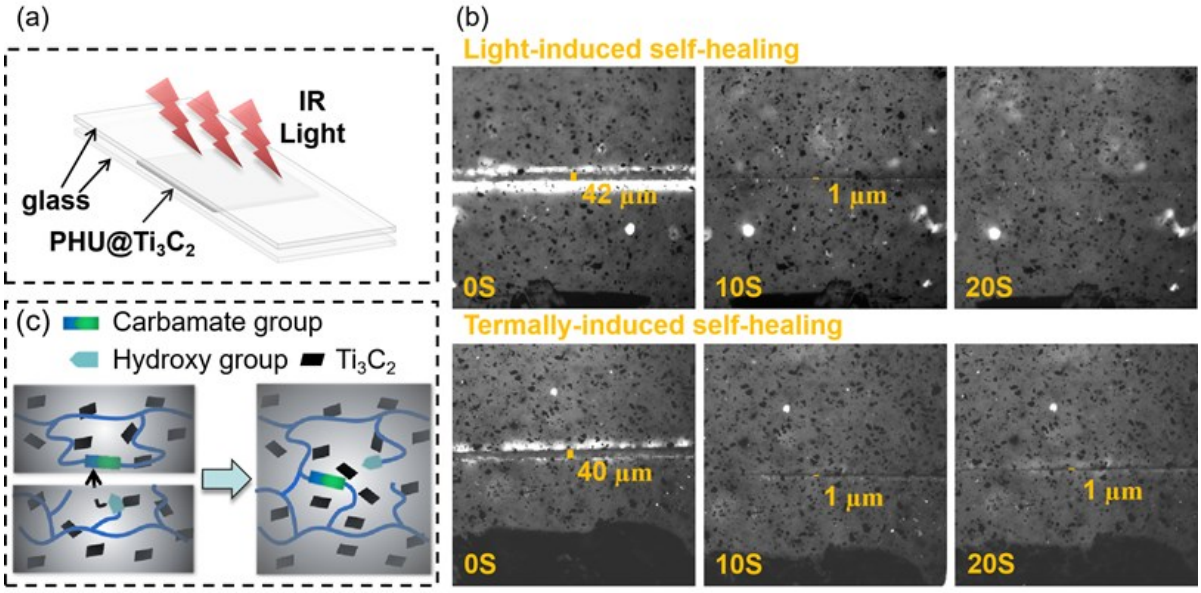

Fig. S13 Thermally/light-induced self-healing of PHU@Ti_3C_2. (a) Schematic diagram of PHU@Ti_3C_2 self-healing experiment. (b) Scratch self-healing at 160ºC or under IR light monitored by polarizing microscope. (c) Mechanistic diagram of PHU@Ti_3C_2 self-healing.

Discussion of Fig. S13:

In the self-healing experiments, a blade was first used to scratch on the surface of PHU@Ti_3C_2 film, and then the self-healing of the scratches was examined by polarized light microscopy at 160ºC and

infrared light irradiation, respectively. The rapid light-induced self-healing of PHU@Ti_3C_2 is attributed to the addition of Ti_3C_2. In contrast to traditional 2D materials, such as GO, rGO, GNs, BN that exhibit only a broad absorption band ranging from UV to NIR region, Ti_3C_2, as one of the MXene's family, usually exhibits two enhanced absorption peaks at visible and near-infrared region due to the localized surface plasmon resonance (LSPR) effect, similar to metal nanoparticles, which results in light absorption enhancement. In addition, Ti_3C_2 have a nearly 100% internal light-to-heat conversion efficiency. (*Adv. Funct. Mater.* **2020**, 2000712; *J. Mater. Chem. A* **2019**, 14319-14327.). Solar energy absorbed by Ti_3C_2 can be efficiently converted into heat emitted into the surrounding medium through lattice scattering vibrations, thus raising the surrounding temperature. Thus, the addition of Ti_3C_2 in PHU can enable efficient transcarbamoylation exchange reactions between hydroxyl groups and carbamates at the crack interface and facilitate the rapid light-induced self-healing of PHU@Ti_3C_2.

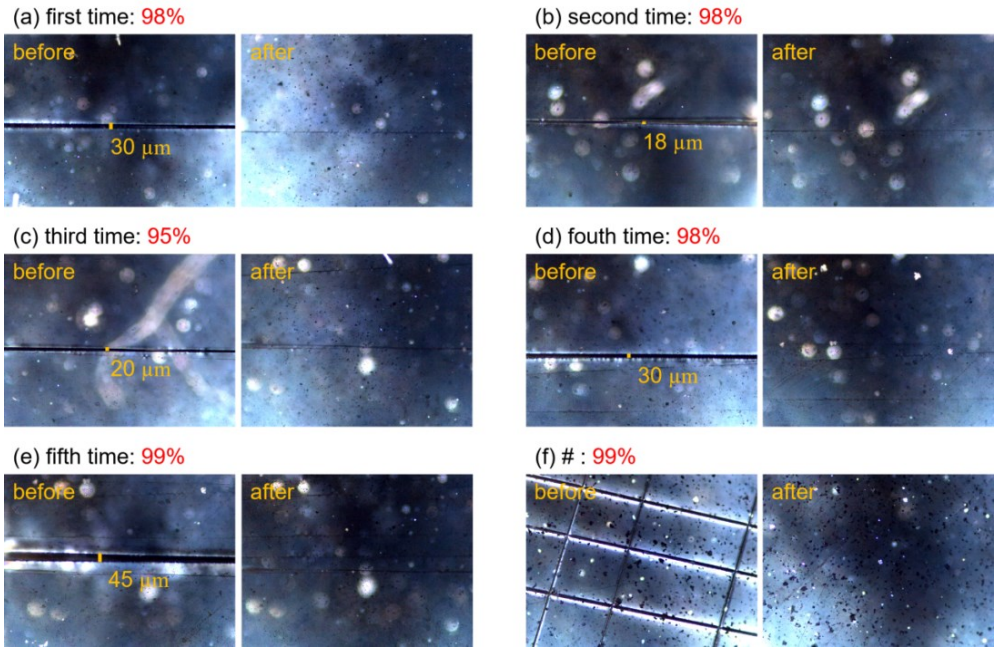

Fig. S14 Scratch self-healing monitoring of PHU@Ti_3C_2 by polarizing microscopy (160ºC, 10s). (a-e) Five cycles of "scratching/self-healing" at roughly the same place of PHU@Ti_3C_2; (f) Self-healing of PHU@Ti_3C_2 with multiple scratches.

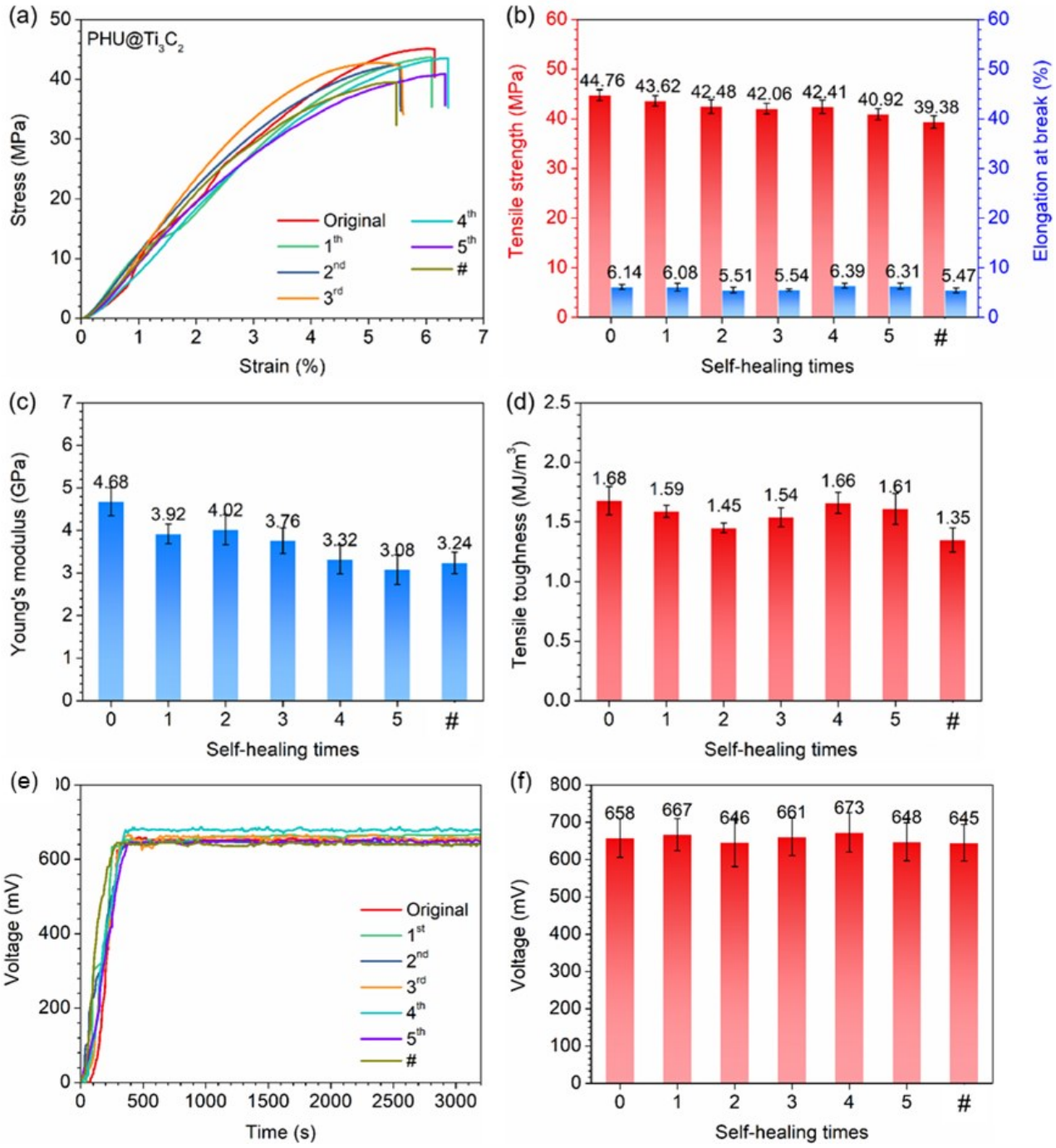

Fig. S15 Mechanical properties and voltage outputs of PHU@Ti_3C_2 after self-healing from damages. (a)-(d) Mechanical properties of PHU@Ti_3C_2 after each instance of self-healing in "scratching/self-healing" cycling experiments; (e) Real-time monitoring of the voltage outputs of PHU@Ti_3C_2-VMEG (Al/Cu) after each instance of self-healing; (f) Stable voltages outputs of PHU@Ti_3C_2-VMEG (Al/Cu) after each instance of self-healing.

Discussion of Fig. S14 and Fig. S15:

Five cycles of "scratching/self-healing" were first performed at roughly the same place of PHU@Ti_3C_2 and the mechanical and output voltage performances of PHU@Ti_3C_2 after each instance of self-healing were investigated. In addition, multiple scratches were made on the surface of PHU@Ti_3C_2 and the corresponding performances after self-healing were also investigated. The experimental results showed that there was only a slight decrease of the mechanical properties after self-healing and no effect on the output voltage properties was observed. This is because that covalent-bond based cross-linking networks can quickly rebuild between the damaged surfaces of PHU@Ti_3C_2 at high temperatures via highly efficient transcarbamoylation reactions between the hydroxyl groups (-OH) and carbamates (-NHCOO-).

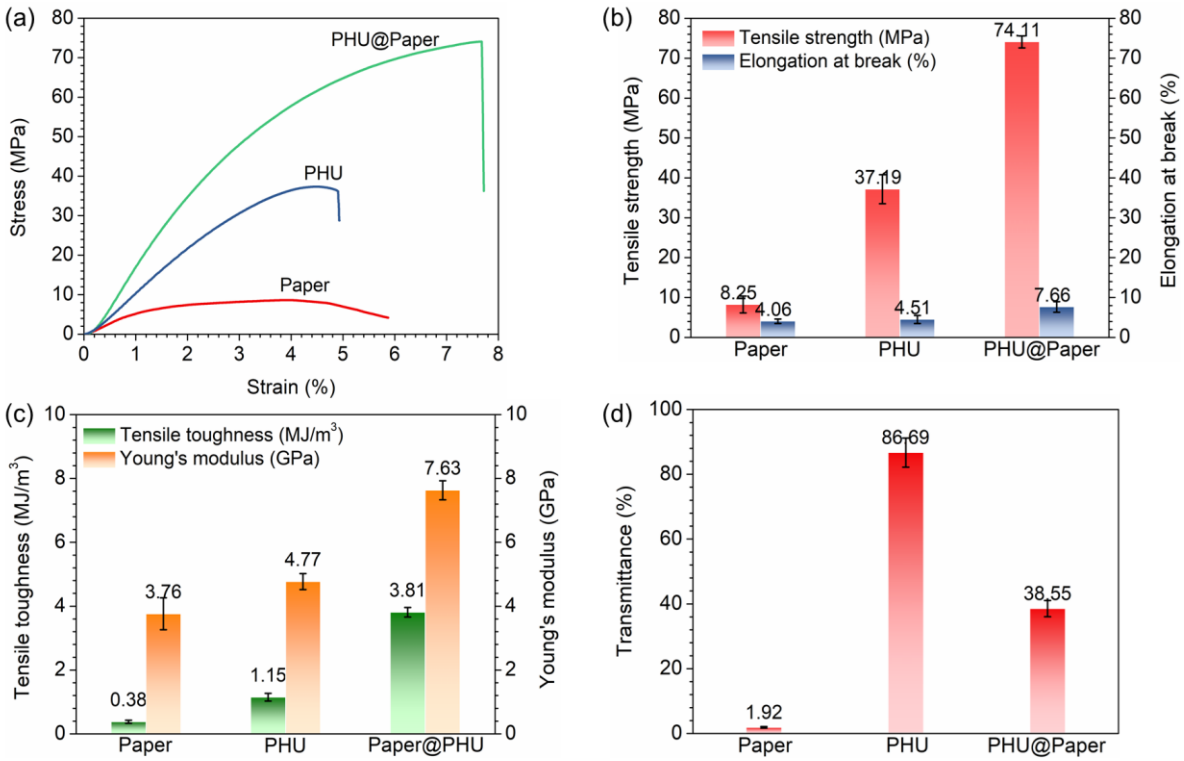

Fig. S16 Mechanical properties and light transmittance of blank paper, PHU and PHU@Paper. (a) Stress-strain curves. (b) Tensile strength and elongation break. (c) Tensile toughness and Young's modulus. (d) Light transmittance.

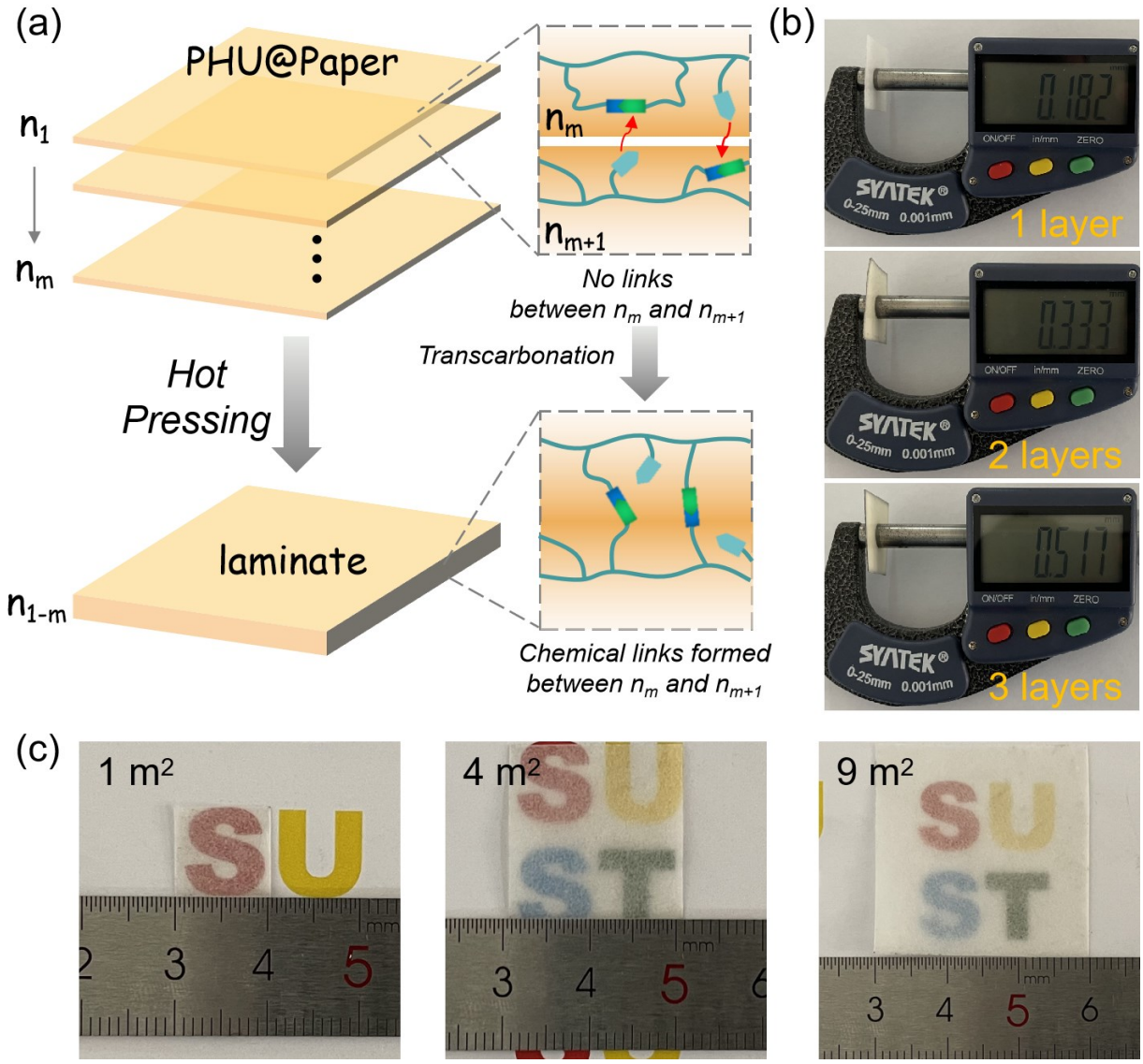

Fig. S17 Preparation of PHU@Paper with different thicknesses and areas. (a) Preparation diagram; (b) Photographs of PHU@Paper with different thickness; (c) Photographs of PHU@Paper with different areas.

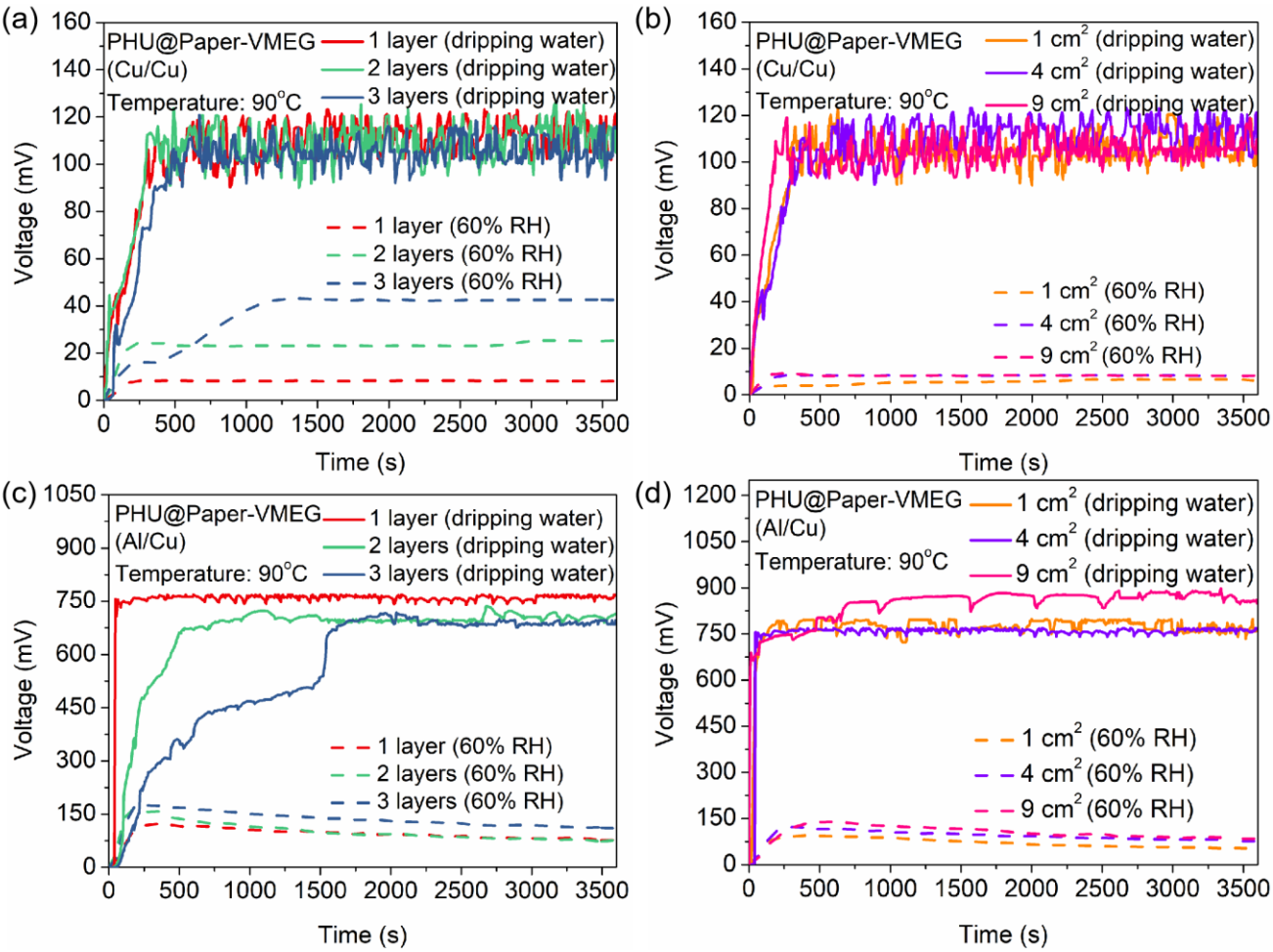

Fig. S18 Electricity generation performance of PHU@Paper-VMEGs with different thicknesses and areas. (a) Voltage output of PHU@Paper-VMEGs (Cu/Cu) with different thicknesses; (b) Voltage output of PHU@Paper-VMEGs (Cu/Cu) with different areas; (c) Voltage output of PHU@Paper-VMEGs (Al/Cu) in different thicknesses; (d) Voltage output of PHU@Paper-VMEG (Al/Cu) in different areas.

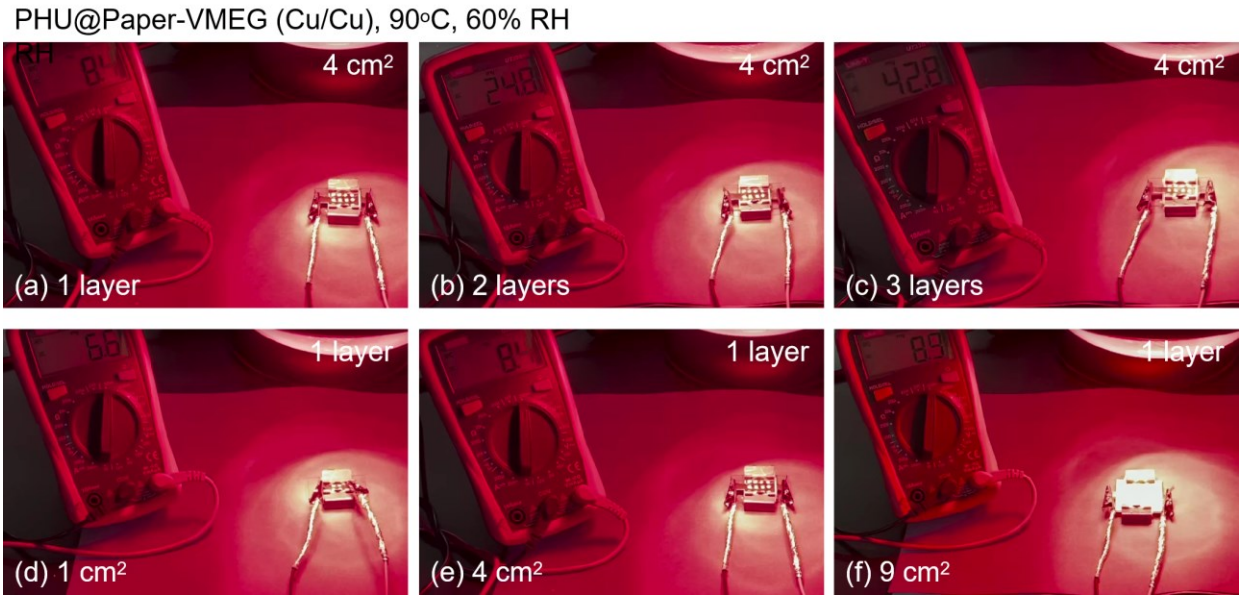

Fig. S19 Voltage output of PHU@Paper-VMEG (Cu/Cu) with different thicknesses and areas (90°C, 60% RH).

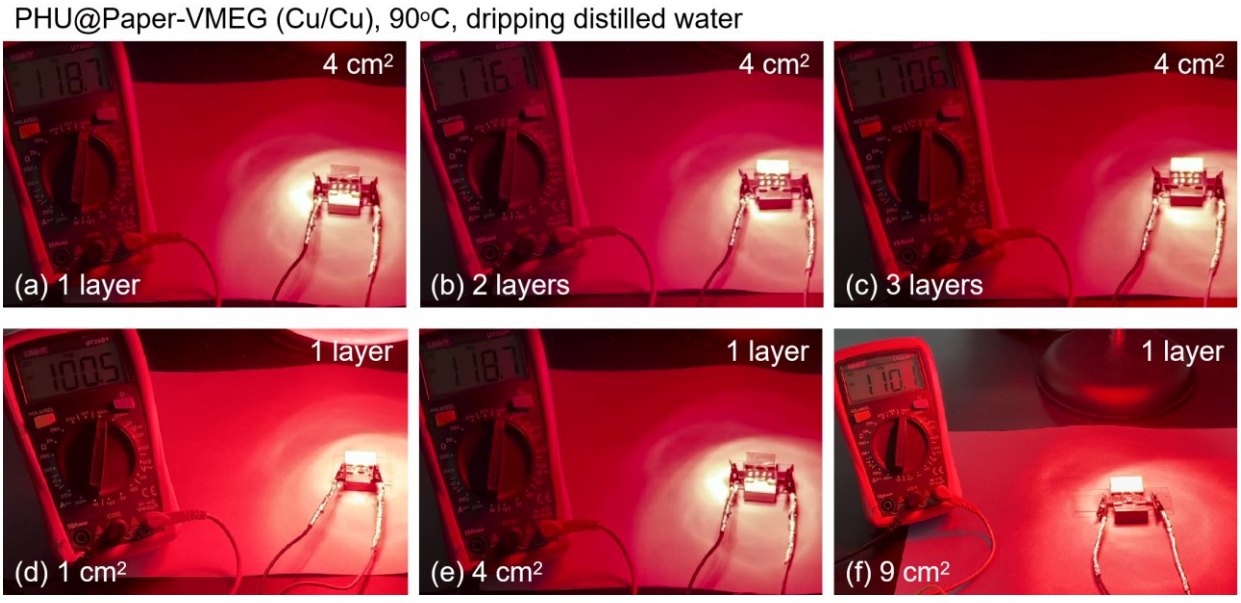

Fig. S20 Voltage output of PHU@Paper-VMEG (Cu/Cu) with different thicknesses and areas (90°C, dripping water).

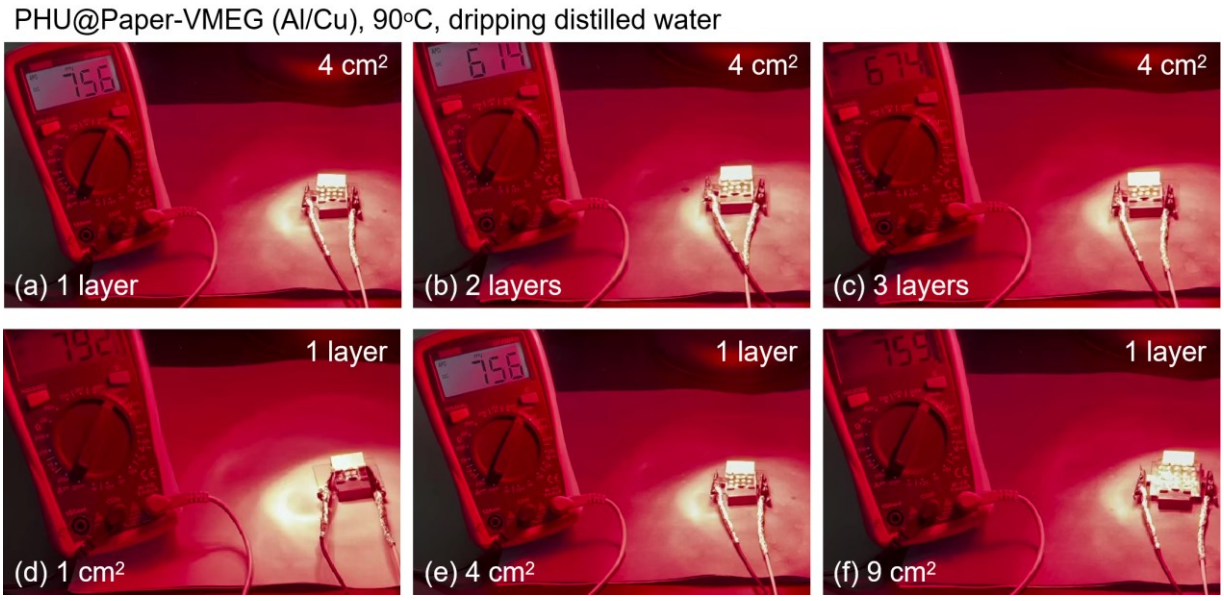

Fig. S21 Voltage output of PHU@Paper-VMEG (Al/Cu) with different thicknesses and areas (90ºC, dripping water).

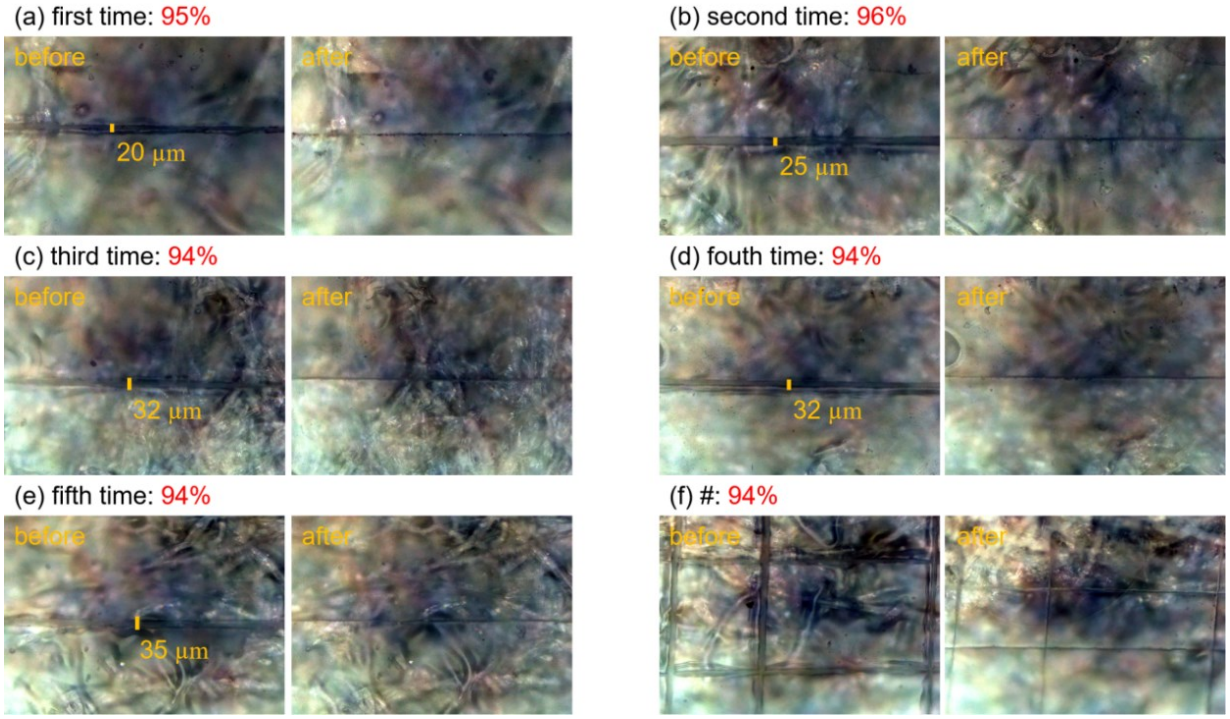

Fig. S22 Scratch self-healing monitoring of PHU@Paper by polarizing microscopy (160ºC, 10s). (a-e) Five cycles of "scratch/self-healing" at roughly the same place of PHU@Paper; (f) Self-healing of PHU@Paper with multiple scratches.

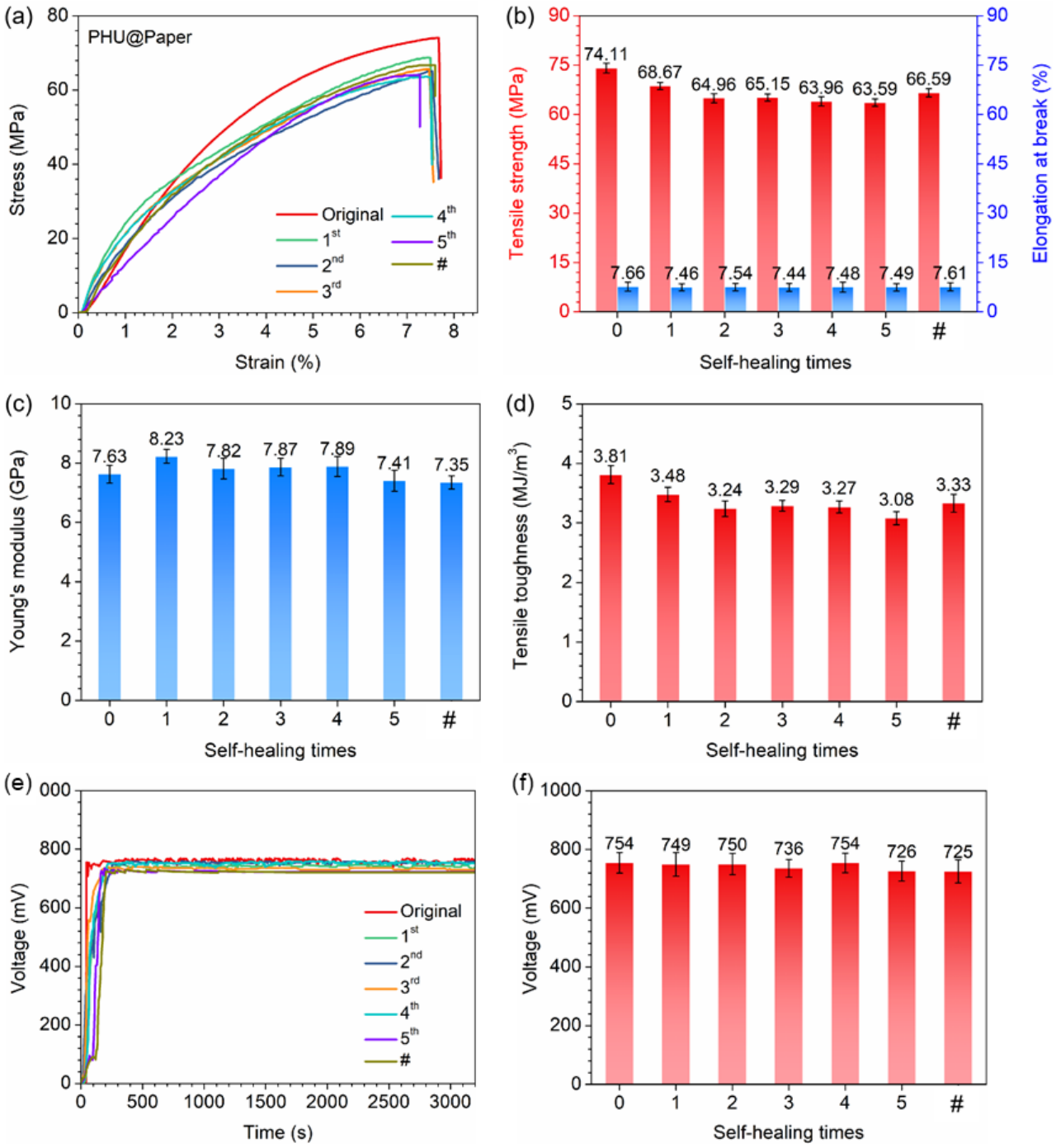

Fig. S23 Mechanical properties and voltage outputs of PHU@Paper after self-healing from damages. (a)-(d) Mechanical properties of PHU@Paper after each instance of self-healing in "scratching/self-healing" cycling experiments; (e) Real-time monitoring of the voltage outputs of PHU@Paper-VMEG (Al/Cu) after each time of self-healing; (f) Stable voltage outputs of PHU@Paper-VMEG (Al/Cu) after each instance of self-healing.

Discussion of Fig. S22 and Fig. S23:

Five cycles of "scratching/self-healing" were first performed at roughly the same place of PHU@Paper and the mechanical and output voltage performances of PHU@Paper after each instance of self-healing were investigated. In addition, multiple scratches were made on the surface of PHU@Paper and the corresponding performances after self-healing were also investigated. The experimental results showed that there was only a slight decrease of the mechanical properties after self-healing and no effect on the output voltage properties was observed. This is because covalent-bond based cross-linking networks can quickly rebuild between the damaged surfaces of PHU@Paper at high temperatures via highly efficient transcarbamoylation reactions between the hydroxyl groups (-OH) and carbamates (-NHCOO-).

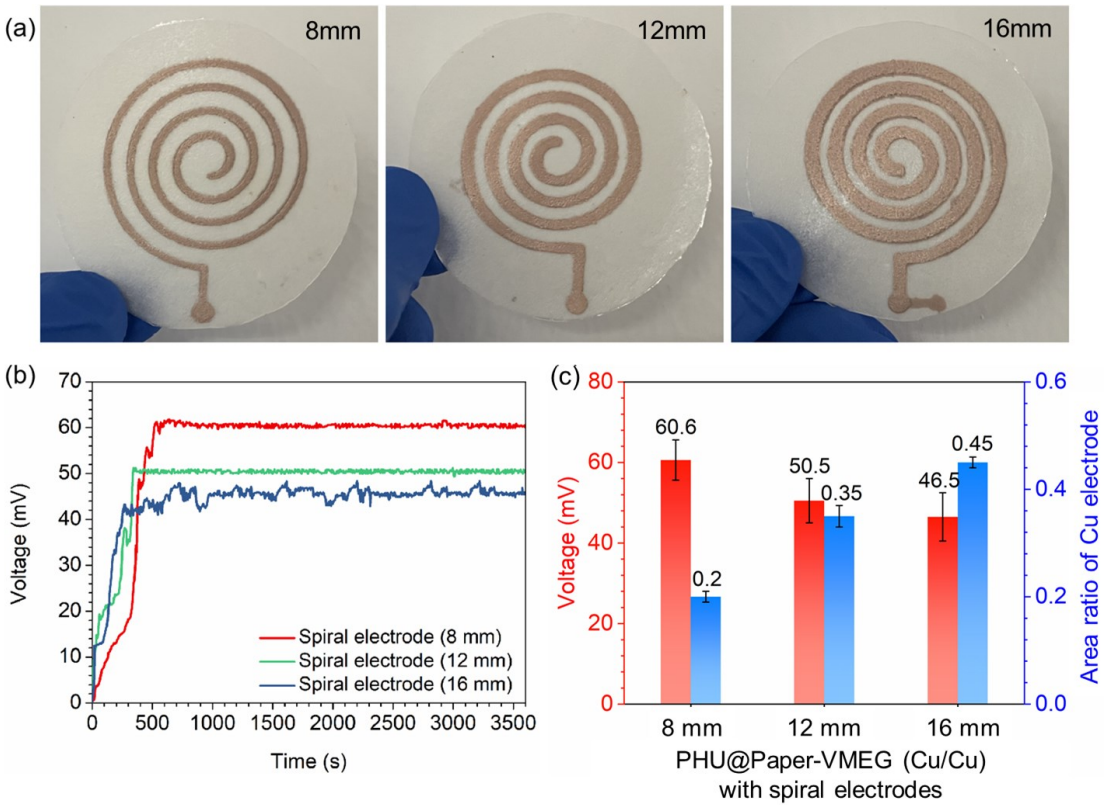

Fig. S24 Effect of the line width of copper electrodes on the voltage output of PHU@Paper-VMEG with spiral electrodes. (a) Photographs of PHU@Paper-VMEG with different line width of spiral copper electrodes. (b) Real-time monitoring of the voltage outputs of PHU@Paper-VMEGs; (c) Stable voltages outputs of PHU@Paper-VMEGs vs. area ratio of copper electrodes (vs. PHU@Paper matrix).

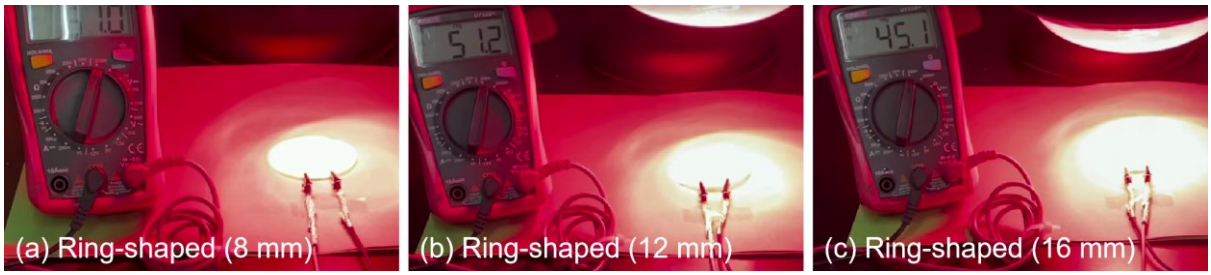

Fig. S25 Voltage output of PHU@Paper-VMEG (Cu/Cu) with different line widths of ring-shaped electrodes. (a) 8 mm, (b) 12 mm, (c) 16 mm.

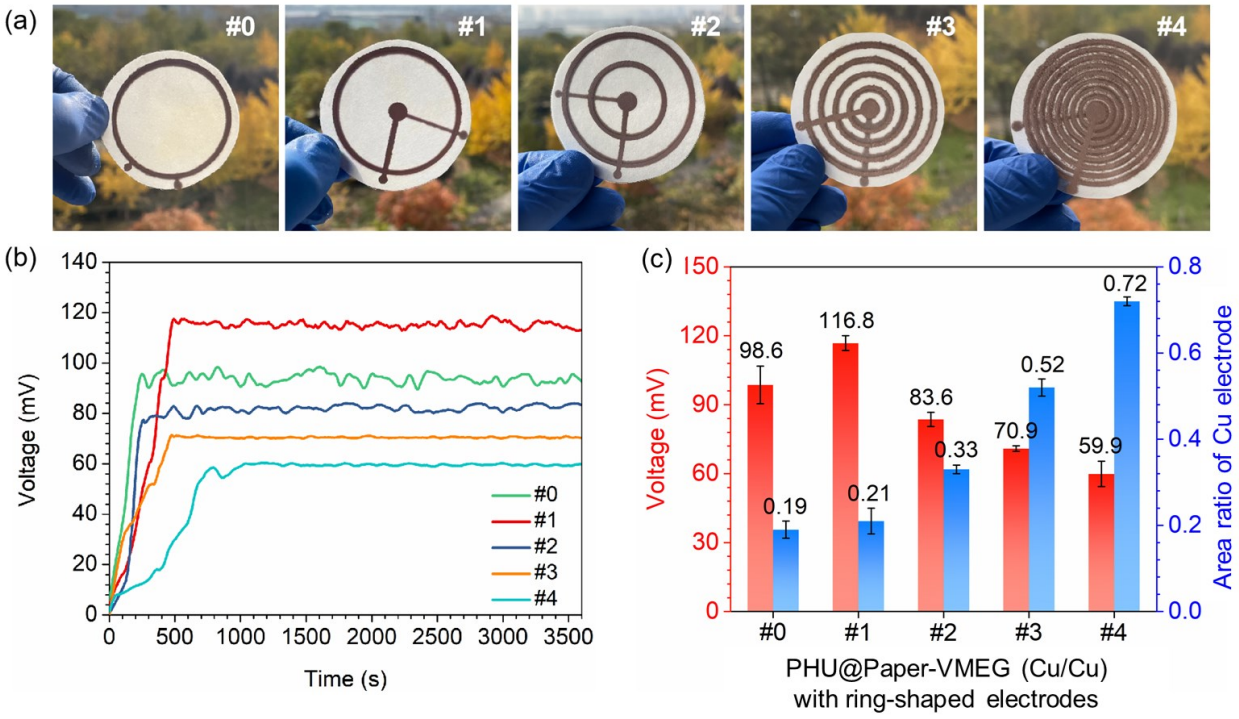

Fig. S26 Effect of the ring number of ring-shaped copper electrodes on the voltage output of PHU@Paper-VMEG. (a) Photographs of PHU@Paper-VMEGs with different ring number of copper electrodes; (b) Real-time monitoring of the voltage outputs of PHU@Paper-VMEGs; (c) Stable voltage outputs of PHU@Paper-VMEGs vs. area ratio of copper electrode (vs. PHU@Paper matrix).

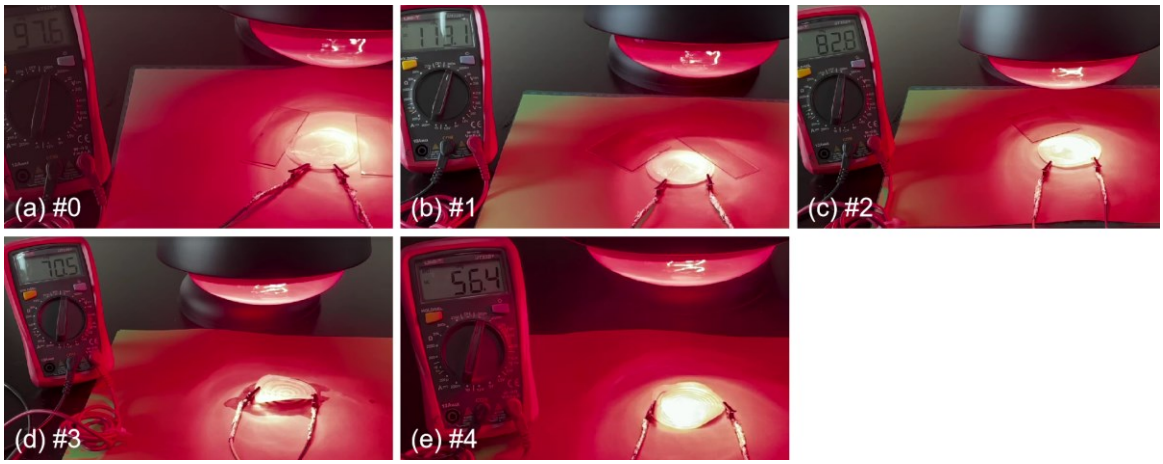

Fig. S27 Voltage output of PHU@Paper-VMEG (Cu/Cu) with different ring number electrodes. (a) #0, (b) #1, (c) #2, (d) #3, (e) #4.

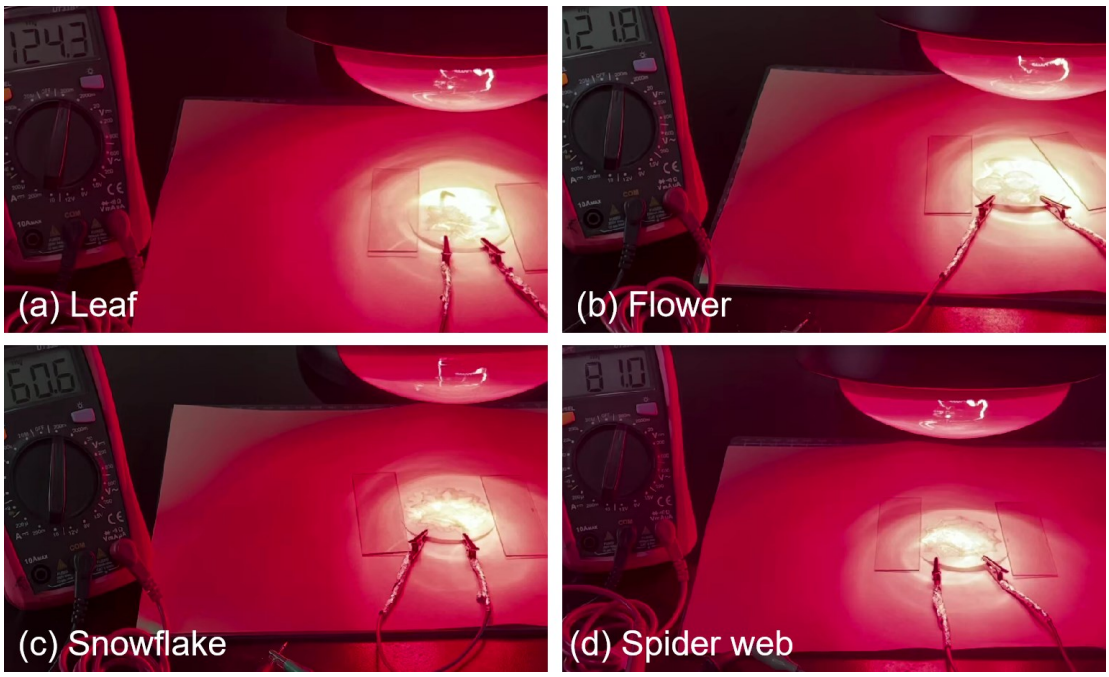

Fig. S28 Voltage output of PHU@Paper-VMEG (Cu/Cu) with different patterns of electrodes (leaf, flower, snowflake and spider web).

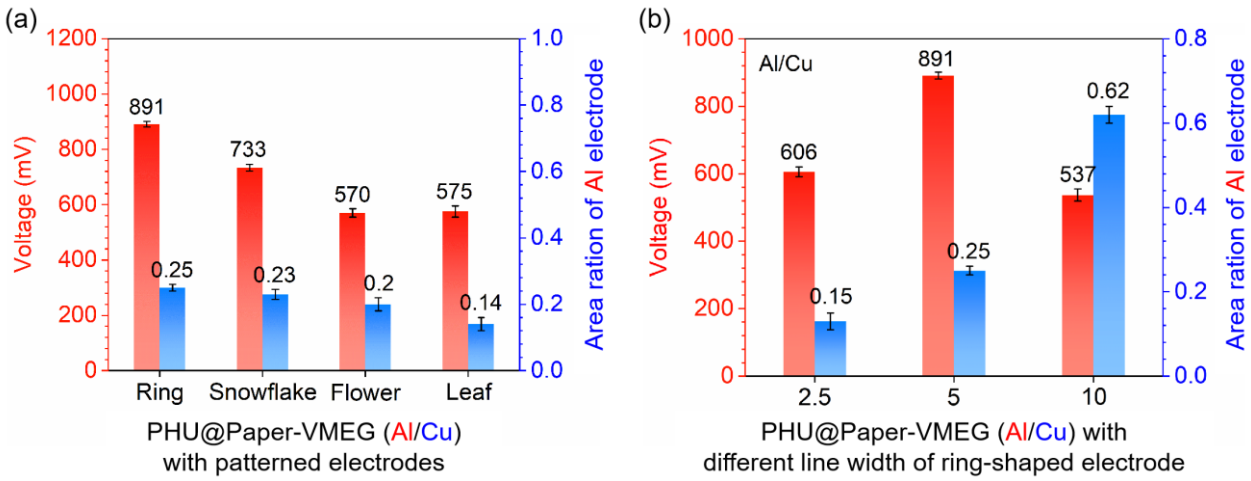

Fig. S29 Effect of Al electrodes on the voltage output of PHU@Paper-VMEG (Al/Cu). (a) Stable voltage output of PHU@Paper-VMEGs (Al/Cu) with patterned electrodes vs. area ratio of Al electrodes; (b) Stable voltage output of PHU@Paper-VMEG with ring-shaped electrodes vs. line width of Al electrode.

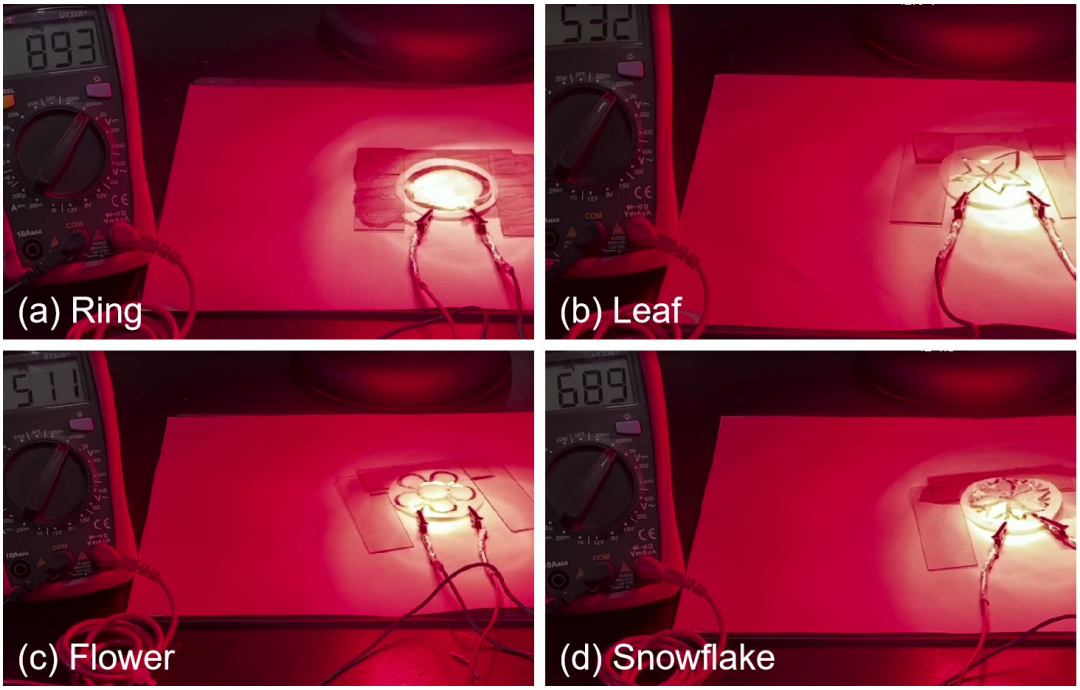

Fig. S30 Voltage output of PHU@Paper-VMEG (Al/Cu) with different patterns of electrodes.

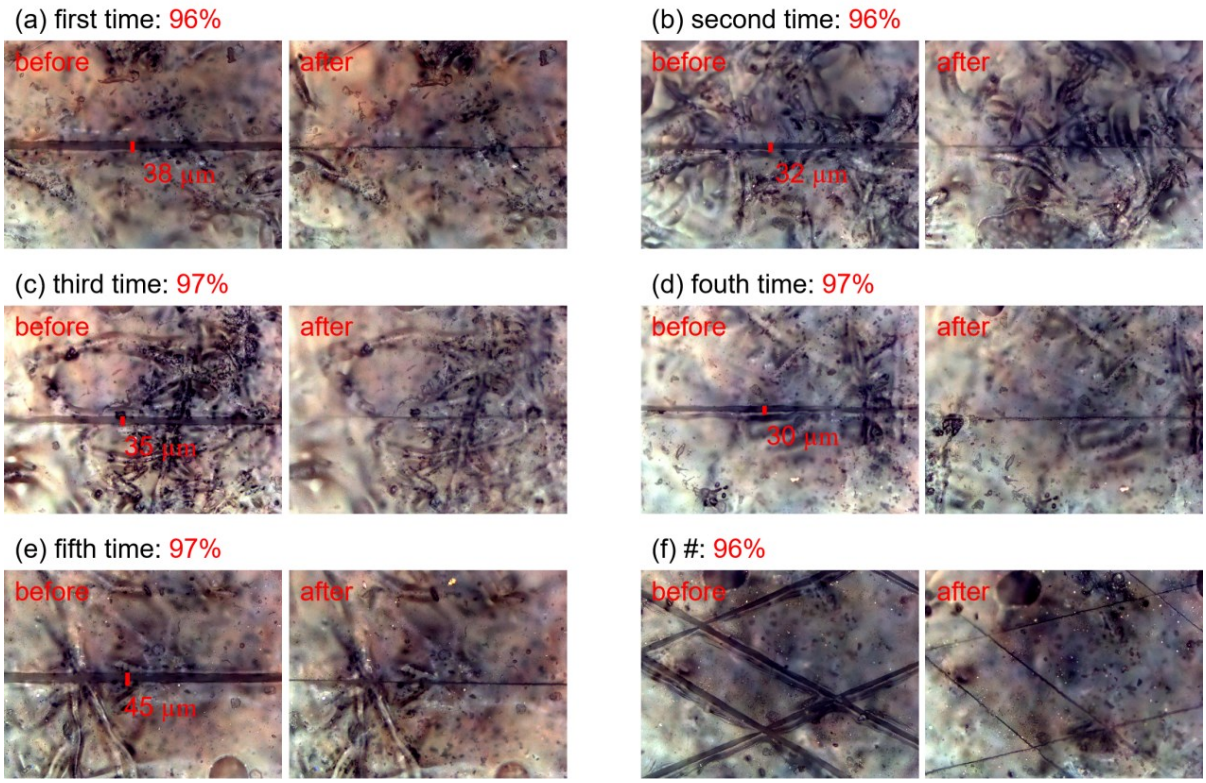

Fig. S31 Scratch self-healing monitoring of PHU@Ti_3C_2 by polarizing microscopy (160ºC, 10s). (a-e) Five cycles of "scratch/self-healing" at roughly the same place of PHU@Ti_3C_2@Paper; (f) Self-healing of PHU@Ti_3C_2@Paper with multiple scratches.

Discussion of Fig. S31 and Fig. S32:

Five cycles of "scratching/self-healing" were first performed at roughly the same place of PHU@Ti_3C_2@Paper and the mechanical and output voltage performances of PHU@Ti_3C_2@Paper after each time of self-healing were investigated. In addition, multiple scratches were made on the surface of PHU@Ti_3C_2@Paper and the corresponding performances after self-healing were also investigated. The experimental results showed that there was only a slight decrease of the mechanical properties after self-healing and no effect on the output voltage properties was observed. This is because covalent-bond based cross-linking networks can quickly rebuild between the damaged surfaces of PHU@Ti_3C_2@Paper at high temperature via highly efficient transcarbamoylation reactions between the hydroxyl groups (-OH) and carbamates (-NHCOO-).

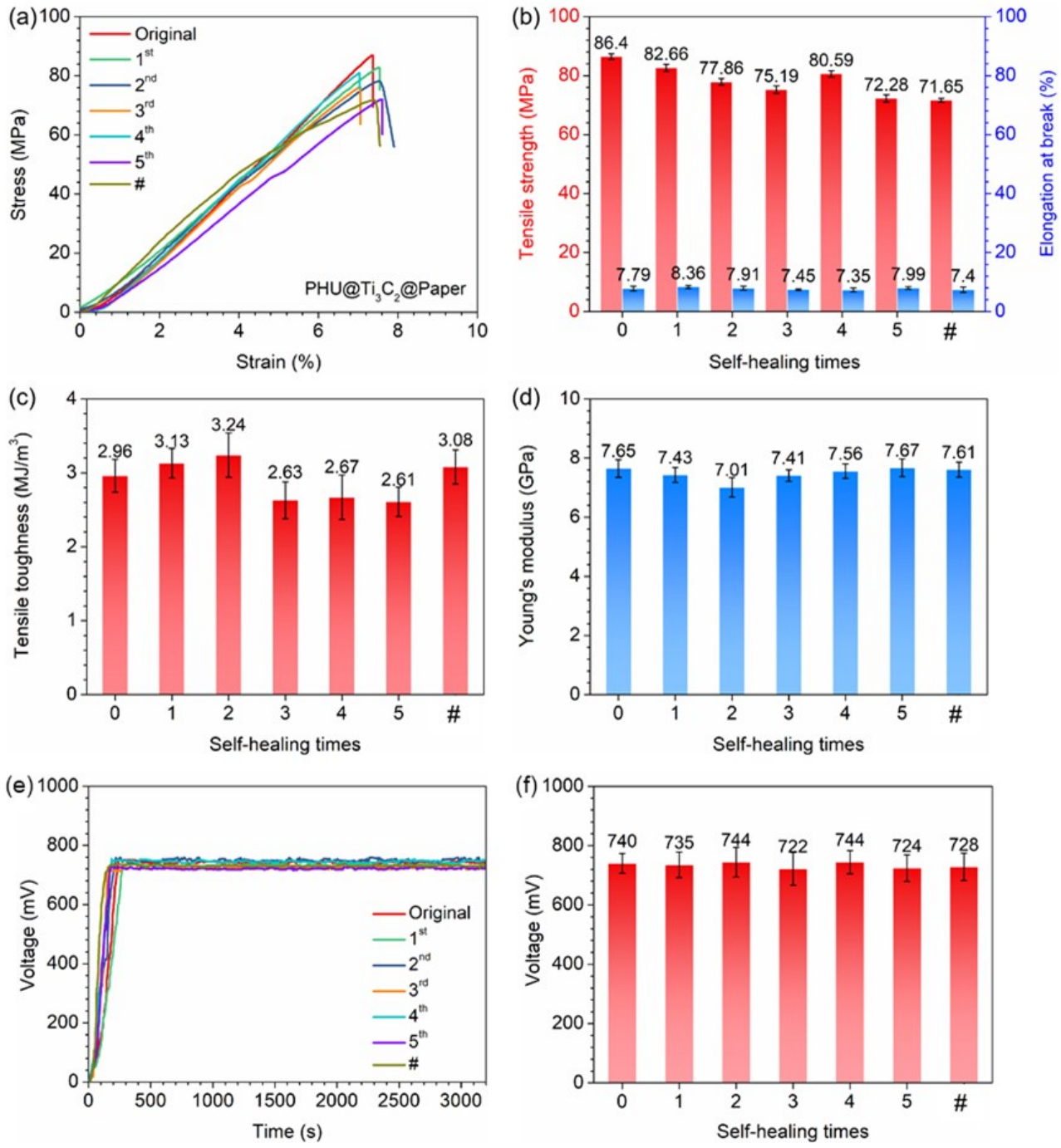

Fig. S32 Mechanical properties and voltage outputs of PHU@Ti_3C_2@Paper after self-healing from damages. (a)-(d) Mechanical properties of PHU@Ti_3C_2@Paper after each instance of self-healing in "scratching/self-healing" cycling experiments; (e) Real-time monitoring of the voltage outputs of PHU@Ti_3C_2@Paper-VMEG (Al/Cu) after each instance of self-healing; (f) Stable voltages outputs of PHU@Ti_3C_2@Paper-VMEG (Al/Cu) after each instance of self-healing.

Table S1 Comparison of VMEG with those reported in the literature.

Active matrix	Electrodes	Voltage /mV	Power Density/ $\mu W/cm^2$	Tensile Strength	Self-healing	Water resistance	Ref. [c]
PSS	Au/Au	800	17	-	No	No	1
PEO	Al/Au	830	24.3	-	No	No	2
PPy	Au/Au	60	0.69	-	No	No	3
HCl/PVA	CNT/CNT	348	47	-	No	No	4
Gelation	Al/Cu	710	5.5	-	No	No	5
PSS/PVA	AgNW/AgNW	600	7.9	75 MPa	Yes [a]	No	6
PHU@Paper	Al/Cu	740	26	86 MPa	Yes [b]	Yes	This study

Note: [a] Self-healing is based on hydrogen-bonding interaction and is easy to fail under high temperature and high humidity conditions; [b] Self-healing is based on dynamic covalent bond; [c] Refs: (1) *Energy Environ. Sci.*, 2019, **12**, 972-978. (2) *J. Mater. Chem. A,* 2021, **9**, 7085-7093. (3) *Adv. Funct. Mater.*, 2016, **26**, 8784-8792. (4) *Nano Energy*, 2019, **60**, 371-376. (5) *ACS Appl. Electron. Mater.*, 2020, **2**, 780-789. (6) *Nano Energy*, 2020, **67**, 104238.